Application of a hybrid multiphase CFD approach to the simulation of gas–liquid flow at a trapezoid fixed valve for distillation trays

Wiedemann, P.; Meller, R.; Schubert, M.; Hampel, U.;

Originally published:

April 2023

Chemical Engineering Research and Design 193(2023), 777-786

DOI: https://doi.org/10.1016/j.cherd.2023.04.016

Perma-Link to Publication Repository of HZDR:

https://www.hzdr.de/publications/Publ-35851

Application of a hybrid multiphase CFD approach to the simulation of gas–liquid flow at a trapezoid fixed valve for distillation trays

Philipp Wiedemann[a,*], Richard Meller[a], Markus Schubert[a,b], Uwe Hampel[a,c]

[a] *Institute of Fluid Dynamics, Helmholtz–Zentrum Dresden–Rossendorf, Bautzner Landstraße 400, 01328 Dresden, Germany*
[b] *Institute of Process Engineering and Environmental Technology, Technische Universität Dresden, 01062 Dresden, Germany*
[c] *Institute of Power Engineering, Technische Universität Dresden, 01062 Dresden, Germany*

Abstract

In the present contribution, we demonstrate the application of a hybrid multiphase CFD approach, which allows for simulating dispersed phases as well as resolved interfaces within an Eulerian framework, for the flow on distillation trays for the first time. The morphology adaptive multifield two–fluid model is exemplified for continuous gas–liquid flow on a generic tray setup with a single trapezoid fixed valve. Instead of fully resolving its geometry in the computational grid, the gas inlets are emulated by implementing mass and momentum sources that are applied to local cell zones. Different zone types in terms of volume and curtain area are tested and compared. The simulation results are verified with experimental data from a lab–scale test rig with air–water flow. Local phase fractions were measured using a conductivity sensor array. The comparison of simulated and experimental results reveals that the relevant time–averaged and transient flow characteristics can be predicted satisfactorily if at least an approximate representation of the valve's geometry in the computational grid is given. However, local differences are observed among the simulated phase distributions due to the varying cell zone volume and hence maximum intensity of the injected momentum.

*Corresponding author.
Email address: p.wiedemann@hzdr.de (Philipp Wiedemann)

Keywords: distillation tray, fixed valve, morphology adaptive multifield two–fluid model, local source terms, CFD

1. Introduction

The increasing energy supply from renewable sources demands a more flexible operation of separation columns. In this context, tray columns with fixed valves trays are increasingly considered for revamps and new apparatuses, since they cope well with enlarged over and partial load modes when compared to sieve trays, cf. Lockett (1986), Goedecke (2006). However, considering the vast number of valve types and possible arrangements as well as their almost unpredictable impact on the complex liquid–vapor flow, the tray design is a challenging task in practice. This applies particularly in view of the fact that most fixed valves feature directional vapor outlets that may be utilized to guide the flow and to counteract liquid maldistribution and recirculation for the purpose of attaining high separation efficiencies, cf. Bell and Solari (1974), Vishwakarma et al. (2018). Nevertheless, tray design is often based on experience or rule of thumb, cf. Kister (1990), and the corresponding knowledge is usually kept undisclosed in the companies. However, in the context of increasing computational power (Markov, 2014, Waldrop, 2016) for simulating complex flow phenomena along with advanced measurement techniques (Hampel et al., 2020) for experimental validation of the underlying models, the application of computational fluid dynamics (*CFD*) becomes increasingly attractive to support the design process. But since it is still not feasible to resolve all details of the two–phase flow in an industrial–scale facility without high performance computing, customized solutions are required for practical daily use. Therefore, we aim at developing a three–dimensional coarse–grid CFD approach that enables engineers to simulate the most relevant scales of two–phase flow scenarios on fixed valve trays at reasonable computational effort.

Two–phase flow on distillation trays appears in various forms and is usually categorized into five major flow regimes (bubble, froth, spray, cellular foam and emulsion regime, cf. Lockett (1986), Kister et al. (1992)), which are associated with characteristic spatio–temporal distributions of vapor and liquid. Additionally, gradual transitions can occur between these major regimes, cf. Dhulesia (1983), Kister et al. (1992), like for many other two–phase flow phenomena, e.g. pipe flow (Wiedemann et al. (2019)) or bubble columns

(Nedeltchev et al. (2020)). Since the actual form of appearance depends on operating conditions, fluid properties and — quite significantly — on the tray design, the phase distribution and the dynamics of the flow cannot be fully anticipated in the design process already. Moreover, the coexistence of different regimes and phase structures should be assumed for an unbiased simulation. This means that liquid–dominated as well as gas–dominated regions may be present along with dispersed structures of the respective accompanying phase. However, two modeling approaches, which focus either on continuous–continuous or continuous–disperse interactions, are presently well–established for the simulation of gas-liquid flows.

On the one hand, the Volume of Fluid (VoF) model is applied with the aim of resolving interfacial structures that are larger than the computational grid size, e.g. for two–phase flows with large–scale interfaces or in the field of microfluidics. For that purpose, VoF uses a computationally efficient single–field approach for handling the two fluids by a single set of mass and momentum equations. Interfaces are represented by gradients of a so–called color function indicating the phases, cf. e.g. Ho (2017), Wörner (2012). However, this approach is impractical for industrial–scale flows with dispersed structures due to the exceptional computational effort arising from the requirement to resolve the interfacial structures on the grid, see e.g. Malvin et al. (2014) who attempted to simulate the two–phase flow in a 1.213 m i.d. sieve tray column. The authors used cell sizes of $(5 \times 2 \times 2)\,\mathrm{mm}^3$ at least in the active zone of the tray to resolve the most relevant scales resulting already in 3.8×10^6 computational cells when only accounting for half of the actual domain by applying a symmetry boundary condition (BC). The latter simplification is, however, not fully appropriate for assessing highly turbulent three–dimensional flow fields on trays, cf. Jiang et al. (2012). Nevertheless, the VoF model can be the method of choice for detailed investigations of the flow through and around single valves. Alizadehdakhel et al. (2009) used the VoF model for evaluating different geometric versions of a single float valve in a small–diameter column. By assuming a fixed position of the valve and resolving its full geometry in the grid, the authors were able to assess geometry modifications by comparing the simulated gas distribution, interfacial area and pressure drop.

On the other hand, two–phase flows can be treated with the so–called Eulerian–Eulerian or Two–Fluid Model (TFM). Here, the two fluids are interpreted as fully interpenetrating continua assuming that one fluid is dispersed in the other one, e.g. dispersed gas bubbles in a continuous liquid

phase. In the TFM approach, governing equations for the conservation of mass and momentum are established in a phase fraction weighted manner and are solved for both phases, cf. Ishii and Hibiki (2011). Since dispersed structures are not resolved in the computational grid, submodels are formulated to describe the interfacial momentum coupling to account for unresolved interfacial forces like drag, lift, virtual mass etc. Due to the concurring nature of the bubble and froth regime on column trays, the vast majority of simulation studies in this field makes use of the TFM, cf. Vishwakarma et al. (2018). Table 1 summarizes recent studies on TFM simulations of two–phase flows on trays with fixed and/or push valves.

Table 1: Literature on TFM simulation of two-phase flow on valve trays

reference	column i.d.	tray specifications	cell number
Zarei et al. (2009)	1.213 m	171 Mini V–Grid valves	$\approx 4.0 \times 10^5$ (half domain with symmetry BC)
Jiang et al. (2012)	0.574 m	10 triangularly shaped fixed valves	$\approx 5.1 \times 10^5$ (half domain with symmetry BC)
Li et al. (2014a)	0.570 m	sieve tray with 8 mm holes and 28 push valves	$\approx 7.3 \times 10^5$
Li et al. (2014b)	0.540 m	10 fixed valves	$\approx 1.5 \times 10^6$ (half domain with symmetry BC)
Zhao et al. (2018)	0.500 m	9 fixed valves with a push valve and 7 mm holes on top	$\approx 7.0 \times 10^5$ (half domain with symmetry BC)

Only Zarei et al. (2009) performed steady–state simulations directly, while the majority of studies considered the transient nature of the two–phase flow to derive temporally averaged distributions of hold–up and liquid velocity. Jiang et al. (2012) investigated the flow on a tray, in which the main openings of the fixed valves were either oriented in the direction of the main liquid flow or reversely. Li et al. (2014a) studied liquid velocities and hold–up distribution on a sieve tray with push valves. The circular holes of the sieve were approximated by squares due to applying a structured Cartesian grid. The simulations of Li et al. (2014b) focused on the flow evolving from a particular fixed valve design with additional outlets in the valve cover providing an extra pushing effect to the liquid phase. Similarly, Zhao et al. (2018) used the TFM to study the flow on a tray with comparably large fixed valves of 80 mm length with an additional push valve and sieve–like holes in the cover. For meshing this complex geometry cell sizes down to 2 mm were used locally at

the valves. With regard to modeling the unresolved interfacial drag between liquid and the bubble swarm all of the above mentioned studies followed the approach of van Baten and Krishna (2000) and used empirical correlations for estimating the average gas fraction in the froth zone that is used to calculate the local slip velocity. However, while e.g. van Baten and Krishna (2000) and Gesit et al. (2003) applied a well–established literature correlation for their sieve tray simulations, Jiang et al. (2012), Li et al. (2014a,b), Zhao et al. (2018) simply fitted new coefficients for this correlation by regression analysis based on their own experimental data. The obtained coefficients vary significantly across these studies. Thus, no universal validity can be attested. Furthermore, drag at large–scale interfaces is not described properly in this approach leading to inaccuracies, in particular for jetting gas inlets on fixed valve trays as observed in the results of e.g. Jiang et al. (2012). In this context only Li et al. (2014b) included a free surface model to counteract diffusion of the resolved large–scale interface. However, an even more fundamental issue is that the standard TFM suffers from the fact that only one fluid is dispersed in the other one (usually gas in liquid). Thus coexisting regimes, like e.g. froth in the lower region and spray in the upper region of the two–phase zone, cannot be captured accurately at the same time.

In summary, neither the VoF model nor the standard TFM allow for capturing all flow morphologies observable on industrial–scale distillation trays with acceptable computational burden. Therefore, it is desirable to combine the advantages of both models within a hybrid approach, cf. Hänsch et al. (2012), Frederix et al. (2021), Colombo et al. (2022). Recently, Meller et al. (2021) proposed a morphology adaptive multifield two–fluid model that is capable of handling both types of interfacial structures — those being smaller than the computational grid size, as well as those, which are larger — within in a single computational framework. More precisely, four numerical phases (continuous gas, continuous liquid, dispersed gas, dispersed liquid) can be considered here and an individual treatment of their interactions is applied with appropriate models in a VoF–like or TFM–like manner depending on the local composition of the phase mixture, i.e. the local flow morphology. In principle, this hybrid approach enables the prediction of two–phase flow on distillation trays without prior assumptions of the actual flow structure. The public source code of this morphology-adaptive multifield two-fluid model is provided by Schlegel et al. (2022).

The present contribution describes the application of Meller's hybrid model (Meller et al., 2021) for the gas–liquid flow on a generic distillation

tray with a single fixed valve. For the sake of reduced computational effort along with the objective of using coarse grids for industrial–scale simulations in future, local mass and momentum sources are used to mimic the gas injection through the valve instead of resolving its full geometry with the computational grid. While our previous contribution (Wiedemann et al., 2022) verified the applicability of this approach and revealed that oscillating sources are needed to properly reproduce the dynamics of the gas injection, the present study focuses on the geometrical representation of the valve. Therefore, different sizes of the cell zones, in which the gas is injected, are investigated with respect to the resulting phase distribution near the valve. Temporally averaged phase contours and liquid velocity fields as well as transient characteristics are compared among the different cases and against experimental data.

2. Modeling approach

The applied morphology adaptive modeling framework is able to handle dispersed as well as resolved interfacial structures, which may coexist in the computational domain, with the same set of equations, cf. Meller et al. (2021). It is essentially based on an Eulerian multifield two–fluid model, in which phase specific, ensemble averaged transport equations are formulated. The governing equations for each numerical phase i are given by the conservation of mass

$$\frac{\partial \left(\alpha_i \varrho_i\right)}{\partial t} + \nabla \cdot \left(\alpha_i \varrho_i \vec{v}_i\right) = \dot{m}_{i,S} \tag{1}$$

and momentum

$$\begin{aligned} &\frac{\partial \left(\alpha_i \varrho_i \vec{v}_i\right)}{\partial t} + \nabla \cdot \left(\alpha_i \varrho_i \vec{v}_i \otimes \vec{v}_i\right) \\ =& -\alpha_i \nabla p + \nabla \cdot \left(2\alpha_i \mu_i \bar{\bar{S}}_i\right) + \alpha_i \varrho_i \vec{g} + \vec{f}_i^{\,\sigma} + \vec{f}_i^{\,MT} + \vec{f}_{i,S} \; . \end{aligned} \tag{2}$$

Here, α_i denotes the volumetric phase fraction of each phase i adding up to unity across all phases. ϱ_i and $\vec{v}_i$ are the density and velocity of phase i, respectively. The pressure p is shared among all phases. μ_i is the effective dynamic viscosity, $\bar{\bar{S}}_i$ the strain rate tensor and $\vec{g}$ the gravitational acceleration.

$\vec{f}_i^{\sigma}$ represents the surface tension force, which is only applied to interfaces of continuous–continuous phase pairs and modeled according to Brackbill et al. (1992). $\vec{f}_i^{MT}$ summarizes the interfacial momentum transfer. For unresolved momentum transfer in continuous–disperse phase pairs $\vec{f}_i^{MT}$ includes closure models for drag, lift, virtual mass, turbulent dispersion and wall lubrication, which are chosen according to Liao et al. (2019). In contrast, for resolved interfaces of continuous–continuous phase pairs $\vec{f}_i^{MT}$ includes drag only. In this case, the model of Štrubelj and Tiselj (2011) is applied in connection with a very low interfacial relaxation time, which ensures a no–slip condition at the interface. The closure models for the interfacial momentum transfer $\vec{f}_i^{MT}$ are immutably selected for pairs of either continuous–continuous or continuous–dispersed phases based on the fixed roles of the individual phases, i.e. each individual phase is designated to be either of dispersed or of continuous morphology, cf. Meller et al. (2021). However, as the present study focuses on the influence of injecting continuous gas into the continuous liquid phase, dispersed phases are neglected here. In order to account for gas injection through the fixed valve additional sources for mass $\dot{m}_{i,S}$ and momentum $\vec{f}_{i,S}$ are considered in equations (1) and (2), respectively. Note that these are applied locally in the continuous gas phase only, see section 3.2.

3. Simulation setup

3.1. Experimental basis

The computational setup is based on experimental investigations that were performed using the facility shown in figure 1. The experimental facility is made of PMMA and features a rectangular tray of 670 mm length (x–direction = liquid inlet to weir) and 400 mm width (y–direction). The facility is 530 mm high (z–direction) and the top is open to the atmosphere. Both downcomer clearance and weir height were fixed to 50 mm. A single R–FV trapezoid standard fixed valve from *Raschig* (dimensions are depicted in figure 1) with a lift height of 7 mm was installed at the center of the tray, which is defined as the origin of coordinates (x, y, z).

The facility was operated with liquid water (l) and gaseous air (g) at ambient conditions. The liquid flow was driven by a centrifugal pump and measured by a magnetic–inductive flow meter in the feed pipe. A flow rate of $\dot{V}_l = 15.25\,\mathrm{m^3/h}$ was adjusted and kept constant during the experiments, which corresponds to a weir load of $38.1\,\mathrm{m^3/(h\,m)}$ and an average inlet velocity of $v_{l,x} = 0.21\,\mathrm{m/s}$. Gas was supplied by the compressed air line of

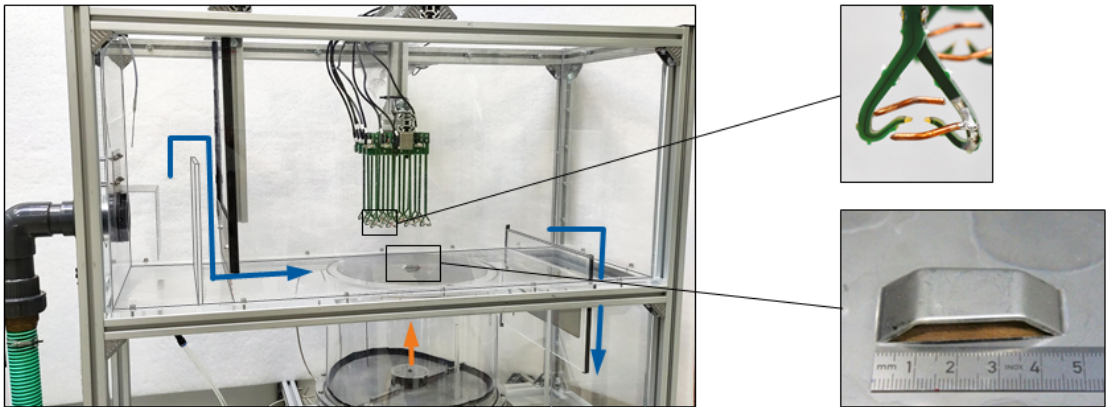

Figure 1: Experimental facility with investigated R–FV fixed valve and conductivity sensor array. Blue and orange arrows indicate flow of liquid and gas, respectively.

the laboratory and adjusted by a mass flow controller. The gas entered the DN400 cylindrical vessel below the tray, see figure 1. After passing a baffle plate to ensure homogeneous distribution in the vessel, the gas passes the centered valve on top of the vessel. Taking into account the local temperature and pressure inside the vessel, a local gas flow rate of $\dot{V}_g = 327\,\mathrm{l/min}$ was obtained in the present experiments. According to the curtain area (CA) of the valve, this yields an average gas velocity of $v_{g,CA} = 11.7\,\mathrm{m/s}$ or in terms of the F–factor $F_{CA} = 12.9\,\mathrm{Pa}^{0.5}$. It should be noted that F_{CA} corresponds to the hole F–factor and not the F–factor being based on the active area, which cannot be defined in a meaningful manner for the present setup.

During the experiments the phase distribution around the valve was measured using the conductivity sensor array shown in figure 1. The sensor is a slightly modified version of the one proposed by Vishwakarma et al. (2021) and is based on the operating principle of a wire–mesh sensor, cf. Prasser et al. (1998). The present sensor is characterized by a new probe tip design featuring additional local shielding and an improved shape to prevent droplet accumulation in the tip region when operating in the spray zone. Local phase fractions were measured with a frequency of 2500 Hz for 60 s of flow time during steady–state operation at various positions around the valve. After time–averaging of the individual data sets the results were merged to form a matrix with $8 \times 8 \times 7$ points with a spacing of $(\Delta x, \Delta y, \Delta z) = (40, 40, 25)\,\mathrm{mm}$ that represents the three–dimensional mean phase fraction distribution. This ma-

trix serves as basis for interpolating phase contours for the comparison with simulation results.

3.2. Computational setup

The experimental facility is captured in the computational setup with its original dimensions as shown in figure 2. However, only 400 mm height are considered above the tray to reduce computational effort.

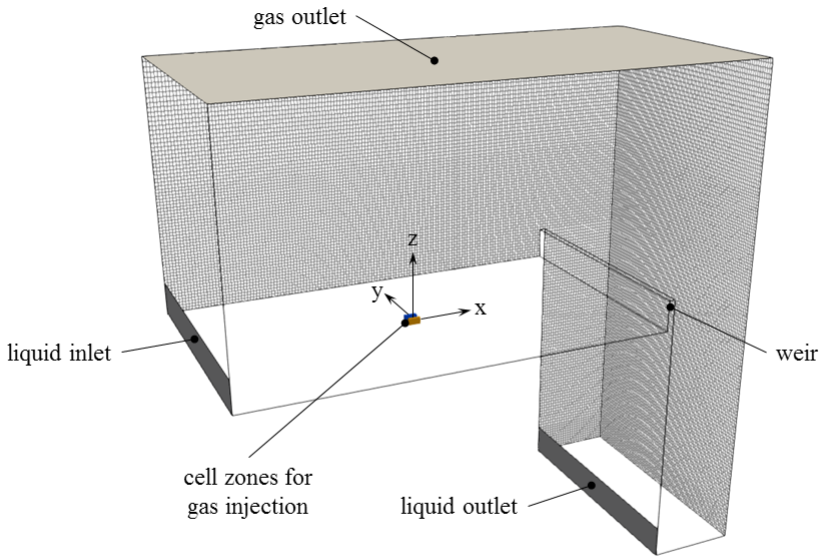

Figure 2: Computational domain with boundary conditions and cell zones for the implementation of local sources

The boundary conditions comprise no–slip at all solid walls, i.e. the tray, all side walls as well as the weir. A homogeneous velocity is assumed at the inlet of the liquid phase, which corresponds to the average experimental value of $v_{l,x} = 0.21\,\mathrm{m/s}$. Such a flat velocity profile has also been used by other authors (cf. Jiang et al., 2012, Li et al., 2014b) and is reasonable when considering the highly turbulent flow in the preceding downcomer, cf. Mehta et al. (1998). For the liquid outlet we apply a so–called matched flow rate condition, which regulates the outlet velocity according to the flow rate at the inlet. In this way, a steady operation point with constant filling level in the downcomer is obtained. The top of the domain is modeled as a standard Neumann type boundary for outflow with optional backflow for the gas phase. For the injection of gas through the curtain area of the valve,

the concept of Wiedemann et al. (2022) is applied, i.e. the gas inlets are mimicked by implementing mass and momentum sources that are applied to local cell zones exclusively (see figure 2). As shown by Wiedemann et al. (2022), dynamic gas injection is required to account for proper dynamics of bubble/jet detachment at the valve, since the complex interaction with the compressible gas volume below is not captured inherently in a single tray simulation. Hence, a sinusoidal gas injection is selected in the present study and the source terms for equations (1) and (2) read

$$\dot{m}_{g,S}(t) = \frac{\dot{V}_g \varrho_g}{2} \left[\sin\left(2\pi f_d t\right) + 1\right] \tag{3}$$

and

$$\vec{f}_{g,S}(t) = \dot{m}_{g,S}(t)\ v_{g,CA} \left[\sin\left(2\pi f_d t\right) + 1\right] \cdot \vec{n}_{CA}\ , \tag{4}$$

respectively. Here, f_d denotes the dominant frequency that was determined from the experimental data by spectral analysis and is associated with the gas detachment frequency. For the operating conditions described in section 3.1 the dominant frequency is $f_d = 7.32\,\mathrm{Hz}$. The factor $1/2$ in equation (3) stems from the fact that the R–FV fixed valve is symmetrical with respect to $y = 0$, see figure 1, and the total gas flow rate is assumed to split equally to the left and right side of the valve. Accordingly, an individual cell zone is considered for each side of the valve. At the same time, this allows for modeling the directional gas injection by means of equation (4), in which $\vec{n}_{CA}$ denotes the face normal vector of the respective curtain area. Due to symmetry solely the sign of the y–component of $\vec{n}_{CA}$ differs between the left and right side of the valve.

For the application of equation (3) it must be considered that (in each time step) the mass flow rate is equally distributed among all grid cells of the selected cell zone. Since the possibilities of representing the valve's geometry by means of cell zones are limited due to the coarse resolution of the computational grid, different scenarios are investigated here, cf. table 2.

All cases are restricted by a minimum lift height of 10 mm and hence overestimate the actual lift height of the valve. While cell zone type a) approximately recovers the real length of the valve, type b) gives the best representation with respect to the curtain area, which is approximated by

Table 2: Overview of investigated cases with different representation of the valve's geometry by cell zones

cell size	$(9.85 \times 10 \times 10)\,\mathrm{mm}^3$		$(10 \times 10 \times 10)\,\mathrm{mm}^3$
cell zone type	a) 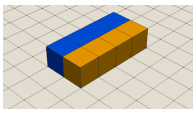	b) 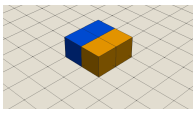	c) 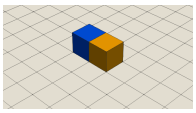
lift height/mm	10	10	10
length/mm	39.4	19.7	10
total curtain area/mm^2	788	394	200
total volume/mm^3	7882	3941	2000

the outer planes in $\pm y$–direction here. Cell zone type c) is equivalent to the extreme case of a point–like source. Note that the total volume of the zone influences the maximum local intensity of the mass flow rate and hence of the momentum source, while the shape of the curtain area affects the mapping of the region of interest.

The investigated scenarios resulted in a total number of 1.36×10^5 computational cells. A time step size of $\Delta t = 5.0 \times 10^{-5}\,\mathrm{s}$ provided a stable convergence behavior for the numerical solution. Details on the numerical solution procedure can be found elsewhere, see Meller et al. (2021).

As a transient process is simulated, the evaluation of the results needs to consider start–up effects that are neglected prior to analyzing field variables. In order to speed up the start–up process in the simulations, the tray region between inlet and weir as well as the downcomer are initialized with liquid, i.e. $\alpha_l = 1$. Previous investigations on the treated single–valve arrangement showed that 5 s of start–up period were sufficient under these conditions, cf. Wiedemann et al. (2022). Moreover, this period represents about 1.5 times the average residence time of liquid on the tray and about 36 events of bubble/jet detachment in the region of interest. Similar values of $(4 \ldots 8)\,\mathrm{s}$ are reported in the literature on simulations of full trays, cf. Jiang et al. (2012), Li et al. (2014a,b). With regard to the subsequent period to be analyzed, 5 s and 10 s were chosen by Jiang et al. (2012) and Li et al. (2014a), respectively. Although our previous study (Wiedemann et al., 2022) revealed almost independent results for an evaluation period of 5 s, too, 10 s are cho-

sen conservatively in the present study for the sake of statistical reliability. Hence, all results in section 4 refer to a flow time of $t = (5 \ldots 15)\,\mathrm{s}$.

4. Results and Discussion

4.1. Analysis of time–averaged phase distribution and liquid velocity

To evaluate the influence of gas injection through the different cell zone types presented in table 2, the resulting distributions of time–averaged phase fractions (holdup) are analyzed. In order to characterize the turbulent two–phase froth zone on temporal average, contours at two levels of the time–averaged gas phase fraction are chosen. The value of $\overline{\alpha_g} = 0.75$ is interpreted as time–averaged interface between froth and pure gas, whereas $\overline{\alpha_g} = 0.25$ is treated as interface between froth and pure liquid. Qualitative differences are already observed in figure 3 depicting the three–dimensional contours of the investigated cases.

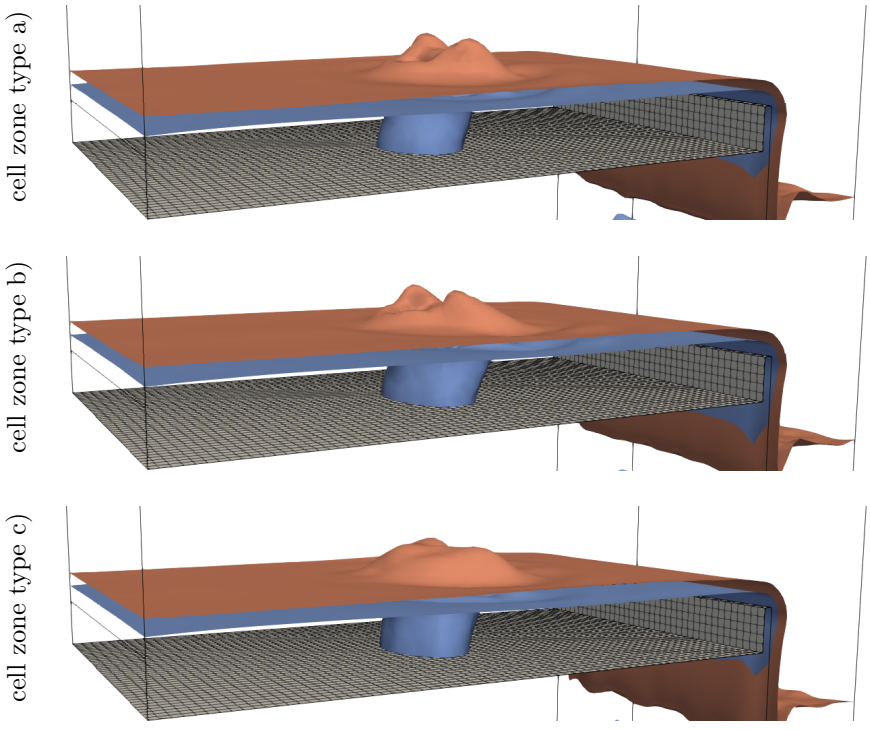

Figure 3: Contours of $\overline{\alpha_g} = 0.75$ (red) and $\overline{\alpha_g} = 0.25$ (blue) for the investigated cell zone types

The froth–liquid interface ($\overline{\alpha_g} = 0.25$) represented by the blue surface forms a hose connecting the tray in the region of the valve with the liquid surface. The girth of this froth hose is predicted to be smallest with the longest injection cell zone (type a) and largest with the intermediate zone length (type b). Due to the liquid flow, this froth structure is inclined towards the liquid downstream direction. That inclination is prominent when using long and intermediate injection cell zones, types a) and b), respectively. However, the short injection cell zone (type c) leads to a weaker inclination of the froth hose. Considering the froth–gas interface ($\overline{\alpha_g} = 0.75$) represented by the red surface, the different cell zone types reveal different qualitative behavior. While the short injection cell zone (type c) produces a flat hill elevated from the free liquid surface, cell zone types a) and b) cause two sharp peaks. Presumably, those are pushed up by the two individual streams of gas originating from the two separated injection cell zones in the numerical setup. The results produced with the long and intermediate injection cell zones, types a) and b), respectively, appear to be qualitatively similar.

Detailed analysis and quantitative comparison are shown below for the lateral distribution near the valve. Since the injected gas contains a velocity component in positive x–direction and is further exposed to drag of the horizontal liquid flow, a slight displacement in positive x–direction is observed for the formed structures in the experiments and simulations. The analysis is hence carried out for two positions downstream of the valve, namely $x = 20\,\mathrm{mm}$ and $x = 60\,\mathrm{mm}$, cf. figures 4 and 5.

Considering the liquid–froth interface ($\overline{\alpha_g} = 0.25$) at $x = 20\,\mathrm{mm}$ in figure 4 the long injection cell zone, type a), delivers the narrowest froth hose, which confirms the observation from the three–dimensional surfaces. This can be explained by the fact, that injecting a given mass flow rate into a larger volume, i.e. cell zone, results in a lower injection velocity and hence in a lower momentum injection compared to a smaller injection cell zone, such as types b) or c). That leads to a widening of the froth hose with the latter two types of injection zone. All types of injection zones reveal a wider froth hose compared to experimental observations. A feature, which is only predicted with the long injection zone (type a) is the presence of two large gas jets ($\overline{\alpha_g} = 0.75$) originating from the tray next to the locations of gas injection and reaching the altitude of the free liquid surface. An explanation for this phenomenon is the comparably low amount of injected momentum as described before for cell zone type a), which does not deliver enough energy to instantly break up larger gas structures as it is the case for injection zone

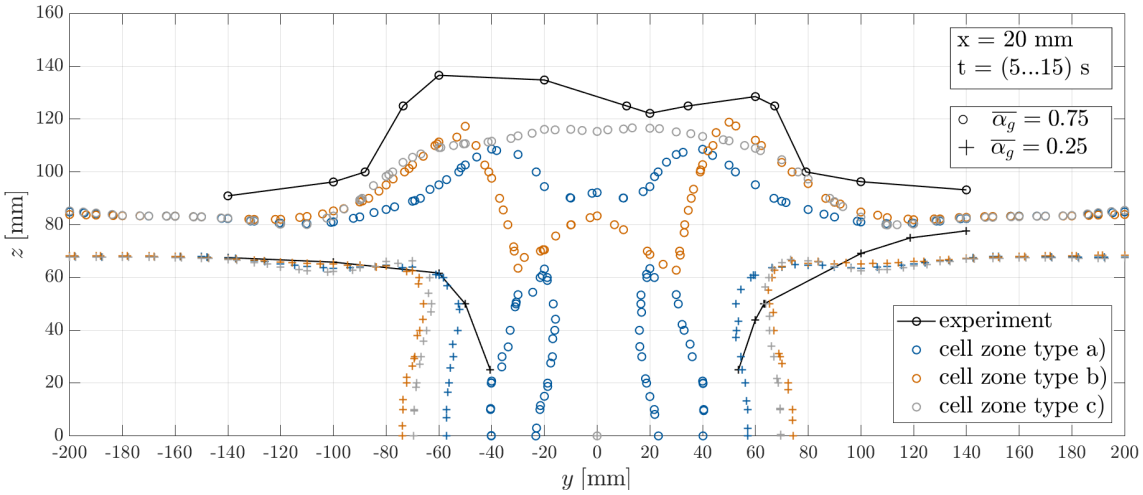

Figure 4: Comparison of time averaged phase distribution from simulation with different cell zones against experiment at $x = 20\,\mathrm{mm}$

types b) and c). Hence, with type a) injection cell zones the gas structures exist longer and, therefore, are more compact and hereby become visible as liquid–froth interface. The experimental data do not show such large–scale gas structures attached to the injection valves. However, jet formation and detachment were also observed visually in the experiments, but is not seen in the experimental data due to the coarse resolution of the sensor with a low number of grid points for the interpolation of the phase contour in this region. For the upper froth–gas interface ($\overline{\alpha_g} = 0.75$) the observations from the three–dimensional surfaces are confirmed as well, such that the double peak structure occurs for the long and intermediate injection zones, types a) and b), respectively, while the short injection zone (type c) delivers a flat hill. The experimental data show such a double peak structure which is much more shallow compared to the simulation results of cell zone types a) and b), while the absolute elevation of the froth–gas interface is measured to be slightly larger compared to the computational results for all injection zone types under investigation. In the results obtained with cell zone type b) a relatively deep cavity of the froth–gas interface is observed between both peaks, which is neither seen with the other injection zone types nor in the experiment. The lateral expansion of the upper froth contour is predicted reasonably well in all simulations. Further away from the region of gas injection, i.e. $y < -120\,\mathrm{mm}$ and $y > 120\,\mathrm{mm}$, the levels of both liquid–froth

and froth–gas interfaces are insensitive to the choice of the cell zone type for gas injection. Therefore, a spatially limited influence of the zone type is attested. However, compared to experimental data the simulated interfaces are located slightly below the experimentally measured ones.

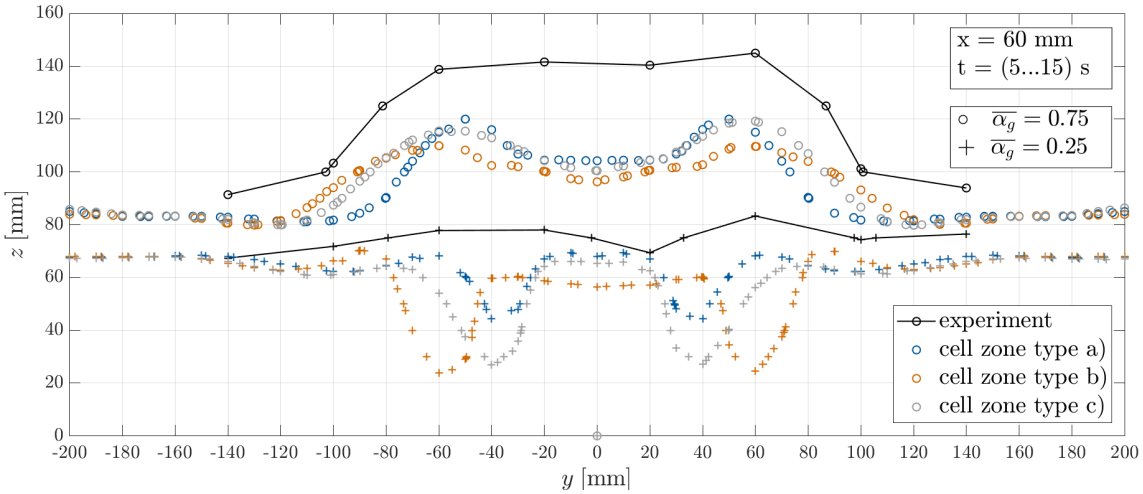

Figure 5: Comparison of time averaged phase distribution from simulation with different cell zones against experiment at $x = 60\,\mathrm{mm}$

At $x = 60\,\mathrm{mm}$ (see figure 5) the different injection zone types reveal qualitatively similar results for the location of the time–averaged froth–gas interface ($\overline{\alpha_g} = 0.75$) showing two comparably flat peaks. However, the gradient of the interface height is predicted to be steeper with type a) injection zones compared to types b) and c). The elevation of the froth–gas interface measured in the experiment is, again, larger than in the simulation results and a flat hill structure is observed rather than a two peaks. Also shape and location of the liquid–froth interface ($\overline{\alpha_g} = 0.25$) are qualitatively similar among all simulation setups showing two small cavities. The cavities are predicted to be similarly deep with cell zone types b) and c), while type a) results in more shallow structures here. The distance between those cavities are similarly small for cell zone types a) and c), while being larger for type b). The cavities cannot be observed in the experimental data.

In order to further evaluate the local effect of the different zone types, the time–averaged liquid velocity field is investigated on the horizontal plane $z = 5\,\mathrm{mm}$, i.e. in the lowest cell layer directly on the tray. In figure 6 results

are presented in terms of contours of velocity magnitude and vector fields for all three cell zone types studied.

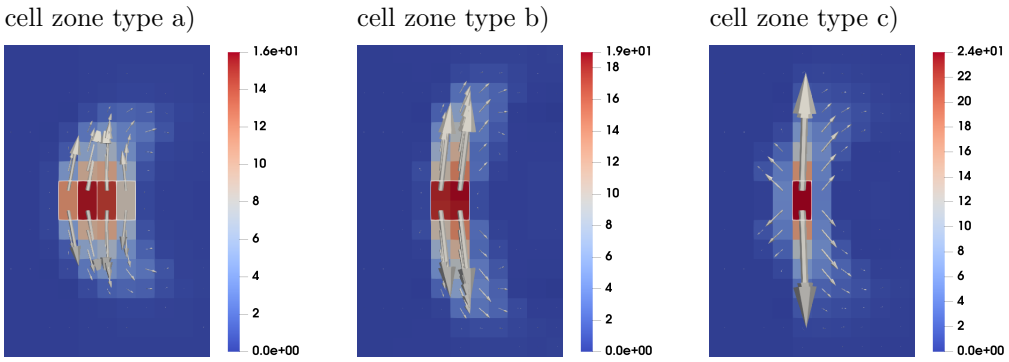

Figure 6: Contours and vectors of time–averaged liquid velocity in m/s at $z = 5\,\mathrm{mm}$ above the tray (main liquid flow direction from left to right, the cell zone for gas injection is marked with white contours)

In accordance with the direction of gas injection through the valve, the liquid is accelerated in opposite lateral directions via gas–liquid momentum transfer in all cases. However, with increasing distance from the injection location the effect rapidly decays until the liquid flow appears completely unaffected after approximately $(40 \ldots 50)\,\mathrm{mm}$ from the curtain area. Thus, the liquid flow is increasingly bent towards the downstream direction of the liquid background flow. According to the biggest length of injection zone type a) the affected region of laterally accelerated liquid is the longest among the investigated cases. The shorter the injection cell zones with types b) and c), the larger is the injection velocity due to the fixed injection gas flow rate. With cell zone type c) the maximum liquid velocity observed at $z = 5\,\mathrm{mm}$ is roughly 50 % larger than with type a). The injected gas locally displaces the liquid and for cell zone type c) this effect becomes so strong that a significant local backflow is observed in the upstream direction of the liquid background flow in front of the cell zone. This may also explain the smaller inclination of the liquid–froth interface ($\overline{\alpha_g} = 0.25$) in figure 3, which probably also leads to accumulating more liquid in the stagnation point to finally fill up the double–peak structure of $\overline{\alpha_g} = 0.75$ observed for type a) and b) in figure 4. However, due to the local concentration of the gas injection in cell zone type c) and the resulting large velocity gradients, the dissipation of kinetic energy is so strong that the liquid velocity quickly decreases with growing distance from the injection zone. Therefore, the pattern of the liquid velocity observed in

the horizontal plane close to the injection valve is quite similar to cell zone types a) and b).

Overall, the qualitative behavior of the system is not excessively influenced by the choice of the injection zone type, if the length of the cell zone is not too short as present for type c). In the latter case, flow features such as a slender froth hose or a double peak of the froth–gas interface cannot be predicted in contrast to longer injection zone types a) and b). Finally, the simulation with cell zone type a) provides the best fit with the experimental data of gas injection through a single fixed valve. However, higher spatial resolution of the experimental data is required in future to obtain more details of the gas–liquid interface and of the flow near the valve, such as gas jets and bubbles.

4.2. Analysis of transient phase fraction characteristics

In addition to the analysis of the time–averaged phase distributions, the transient behavior of the phase fraction is evaluated for two positions near the valve. Here, the closest probe positions slightly downstream of the valve at the lowest sensor elevation of $z = 25\,\mathrm{mm}$ were selected, namely a left probe at $(20, 20, 25)\,\mathrm{mm}$ and a right probe at $(20, -20, 25)\,\mathrm{mm}$. For the analysis a representative time span of $0.5\,\mathrm{s}$ is arbitrarily chosen from the full time series. Figure 7 shows the temporal evolution of the measured and simulated gas fractions.

The experimental time series show almost synchronously fluctuating gas fractions between 0 and 1 in a square pulse fashion, which is attributed to the almost simultaneous formation and detachment of large gas jets or bubbles on both sides of the valve. As the dominant frequency of these fluctuations is directly used in equations (3) and (4) without any time shift, the simulated time series consequently predict similar dynamics. The reasons for deviations on smaller time scale are twofold. Firstly, the superposition with random effects in the real flow, e.g. small bubbles, and other frequencies is not considered in the injection model. Secondly, the volume averaging nature of CFD does not allow for a point–like data acquisition as done in the experiment. The latter may also be the reason for not reaching pure liquid, i.e. $\alpha_g = 0$, in the simulations.

With regard to the different cell zones for gas injection it can be observed from figure 7 that type a) and b) yield an almost constantly repeated oscillation, while much more irregular amplitudes of α_g are obtained for the

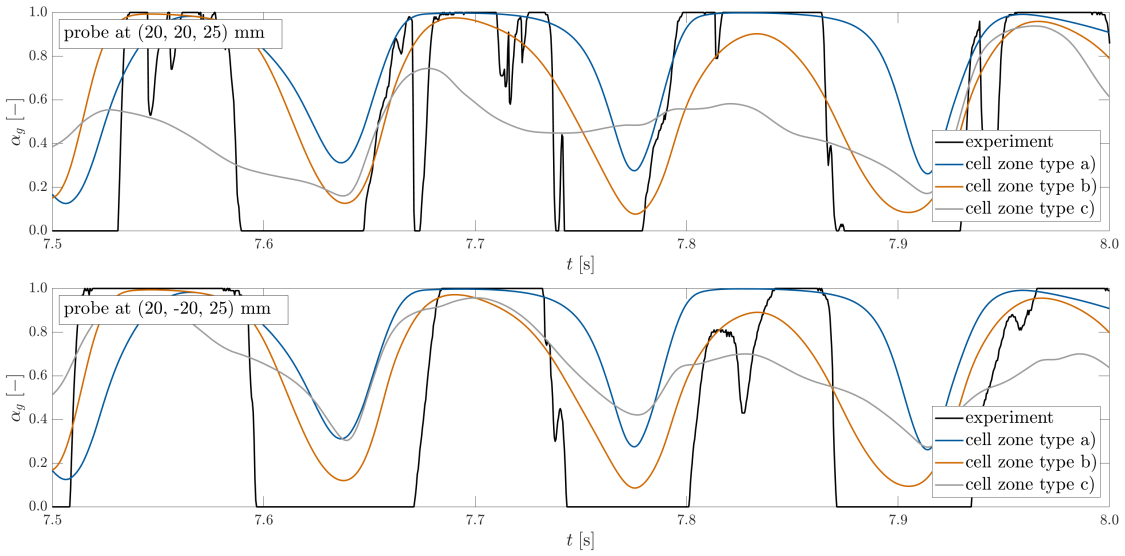

Figure 7: Temporal evolution of gas phase fraction on left (top) and right (bottom) side of the valve

point–like injection with cell zone type c). Moreover, notable differences between the left and right side of the valve are seen for type c), whereas cell zone types a) and b) show a consistent course for both sides. The apparent differences in the duty cycle and also in the overall level between type a) and b) can be explained by the length of these cell zones. With respect to the x–coordinate the probe positions coincide with the downstream end of cell zone type a), but exhibit an offset for the intermediate cell zones of type b). Hence, the gas pulse replaces more liquid locally at the probe positions for type a) when compared to type b). In this way type a) also provides the experimentally observed feature of longer periods with $\alpha_g = 1$. On the other hand, however, the intermediate length of zone type b) provides higher momentum during the injection (see also figure 6), which leads to faster passage of the detached gas and thus better agreement with the shorter experimental duty cycle. Basically, the above argumentation applies also to cell zone type c), since lower gas fractions are observed at the probes (due to the much larger distance to the injection zone) and broader cycles are obtained according to the smaller influence of the momentum source in these points (see figure 6). However, an explanation for the irregular behavior cannot be given here.

When focusing on the abrupt changes between liquid and gas in the experiments, only the long (type a) and intermediate (type b) cell zones provide a reasonably steep increase of the gas fraction at the beginning of each pulse, in particular, when taking volume averaging into account. However, the declining part of the gas pulses is significantly flatter and does poorly agree with the experimental results. A possible reason might be slow bubble detachment, which could be attributed to the neglected but possibly present z–component at the gas inlets, or to a deviating jet or bubble growth rate. Nevertheless, against the background of coarse–grid simulations the application of cell zone types a) and b) leads to a reasonable agreement with the experimentally observed dynamics.

5. Conclusions

A morphology adaptive multifield two–fluid model was used to simulate the two–phase flow on a generic distillation tray setup with a single trapezoid fixed valve. The valve was emulated by the implementation of local mass and momentum sources in the gas phase. Different geometric representations of the valve were investigated in the form of varying size of the cell zones for the gas injection. The comparison of the simulation results with experimental phase fraction data from a conductivity sensor array showed that the formation of the characteristic froth zone is basically accomplished by all investigated cell zone types. However, local differences are observed with respect to mapping the gas injection to the computational grid and due to the resulting intensity of the momentum source. With regard to evaluating the local dynamics of the two–phase flow, the relation between mesh resolution, probe location and size of the gas injection zone plays a crucial role for the analysis. From the present study it can be concluded that at least an approximate representation of the valve's geometry in the computational grid is necessary to properly predict the main characteristics. Point–like implementations of the source terms did not provide reasonable agreement with the experimental data regarding the dynamics.

Based on the current results, future investigations will focus using the full capabilities of the hybrid model in terms of additionally considering dispersed gas and liquid phases. Further, more complex valve geometries as well as multiple valve arrangements need to be studied to transfer the approach to industrial–scale distillation trays in the future.

Acknowledgement

The authors acknowledge technical support by M. Tschofen, R. Franz, M. Löschau and S. Weckesser. The project received funding from the German Federal Ministry for Economic Affairs and Climate Action (BMWK) via the AiF and the Forschungs–Gesellschaft Verfahrens–Technik (GVT) under grant no. 20835 BG. The development of the hybrid multiphase CFD model was supported by the Helmholtz European Partnering Program in the project *Crossing borders and scales (Crossing)*. The fixed valve was kindly provided by Raschig GmbH.

References

Alizadehdakhel, A., Rahimi, M., Alsairafi, A.A., 2009. Numerical and experimental investigation on a new modified valve in a valve tray column. Korean Journal of Chemical Engineering 26, 475–484.

van Baten, J.M., Krishna, R., 2000. Modelling sieve tray hydraulics using computational fluid dynamics. Chemical Engineering Journal 77, 143–151. doi:10.1016/S1385-8947(99)00164-3.

Bell, R.L., Solari, R.B., 1974. Effect of nonuniform velocity fields and retrograde flow on distillation tray efficiency. AIChE Journal 20, 688–695. doi:10.1002/aic.690200409.

Brackbill, J.U., Kothe, D.B., Zemach, C., 1992. A continuum method for modeling surface tension. Journal of Computational Physics 100, 335–354. doi:10.1016/0021-9991(92)90240-Y.

Colombo, M., De Santis, A., Hanson, B., Fairweather, M., 2022. Prediction of horizontal gas–liquid segregated flow regimes with an all flow regime multifluid model. Processes 10, 920. doi:10.3390/pr10050920.

Dhulesia, H., 1983. Operating flow regimes on the valve tray. Chemical Engineering Research and Design 61, 329–332.

Frederix, E., Dovizio, D., Mathur, A., Komen, E., 2021. All-regime two-phase flow modeling using a novel four-field large interface simulation approach. International Journal of Multiphase Flow 145, 103822. doi:10.1016/j.ijmultiphaseflow.2021.103822.

Gesit, G., Nandakumar, K., Chuang, K.T., 2003. Cfd modeling of flow patterns and hydraulics of commercial-scale sieve trays. AIChE Journal 49, 910–924. doi:10.1002/aic.690490410.

Goedecke, R. (Ed.), 2006. Fluidverfahrenstechnik. Wiley-VCH, Weinheim.

Hampel, U., Schubert, M., Döß, A., Sohr, J., Vishwakarma, V., Repke, J.U., Gerke, S.J., Leuner, H., Rädle, M., Kapoustina, V., Schmitt, L., Grünewald, M., Brinkmann, J.H., Plate, D., Kenig, E.Y., Lutters, N., Bolenz, L., Buckmann, F., Toye, D., Arlt, W., Linder, T., Hoffmann, R., Klein, H., Rehfeldt, S., Winkler, T., Bart, H.J., Wirz, D., Schulz, J., Scholl, S., Augustin, W., Jasch, K., Schlüter, F., Schwerdtfeger, N., Jahnke, S., Jupke, A., Kabatnik, C., Braeuer, A.S., D'Auria, M., Runowski, T., Casal, M.F., Becker, K., David, A.L., Górak, A., Skiborowski, M., Groß, K., Qammar, H., 2020. Recent advances in experimental techniques for flow and mass transfer analyses in thermal separation systems. Chemie Ingenieur Technik 92, 926–948. doi:10.1002/cite.202000076.

Ho, M.K.M., 2017. Advances in interface modeling, in: Yeoh, G.H. (Ed.), Handbook of Multiphase Flow Science and Technology. Springer, Singapore, pp. 1–28. doi:10.1007/978-981-4585-86-6_23-1.

Hänsch, S., Lucas, D., Krepper, E., Höhne, T., 2012. A multi-field two-fluid concept for transitions between different scalesof interfacial structures. International Journal of Multiphase Flow 47, 171–182. doi:10.1016/j.ijmultiphaseflow.2012.07.007.

Ishii, M., Hibiki, T., 2011. Thermo-Fluid Dynamics of Two-Phase Flow. Second ed., Springer, New York. doi:10.1007/978-1-4419-7985-8_1.

Jiang, S., Gao, H., Sun, J., Wang, Y., Zhang, L., 2012. Modeling fixed triangular valve tray hydraulics using computational fluid dynamics. Chemical Engineering and Processing: Process Intensification 52, 74–84. doi:10.1016/j.cep.2011.11.009.

Kister, H.Z., 1990. Distillation Operation. McGraw–Hill, Inc., New York.

Kister, H.Z., Haas, J.R., Hart, D.R., Gill, D.R., 1992. Distillation Design. McGraw-Hill, Inc., New York.

Li, Q., Li, L., Zhang, M., Lei, Z., 2014a. Modeling flow-guided sieve tray hydraulics using computationalfluid dynamics. Industrial & Engineering Chemistry Research 53, 4480–4488. doi:10.1021/ie402008c.

Li, X., Yang, N., Sun, Y., Zhang, L., Li, X., Jiang, B., 2014b. Computational fluid dynamics modeling of hydrodynamicsof a new type of fixed valve tray. Industrial & Engineering Chemistry Research 53, 379–389. doi:10.1021/ie400408u.

Liao, Y., Ma, T., Krepper, E., Lucas, D., Fröhlich, J., 2019. Application of a novel model for bubble-induced turbulence to bubbly flows in containers and vertical pipes. Chemical Engineering Science 202, 55–69. doi:10.1016/j.ces.2019.03.007.

Lockett, M.J. (Ed.), 1986. Distillation tray fundamentals. Cambridge University Press, Cambridge.

Malvin, A., Chan, A., Lau, P.L., 2014. Cfd study of distillation sieve tray flow regimes using the droplet size distribution technique. Journal of the Taiwan Institute of Chemical Engineers 45, 1354–1368. doi:10.1016/j.jtice.2014.01.002.

Markov, I.L., 2014. Limits on fundamental limits to computation. Nature 512, 147–154. doi:10.1038/nature13570.

Mehta, B., Chuang, K.T., Nandakumar, K., 1998. Model for liquid phase flow on sieve trays. Transactions of the Institution of Chemical Engineers 76, 843–848.

Meller, R., Schlegel, F., Lucas, D., 2021. Basic verification of a numerical framework applied to a morphology adaptive multifield two-fluid model considering bubble motions. International Journal for Numerical Methods in Fluids 93, 748–773. doi:10.1002/fld.4907.

Nedeltchev, S., Top, Y., Hlawitschka, M.W., Schubert, M., Bart, H.J., 2020. Identification of the regime boundaries in bubble columns based on the degree of randomness in the signals. The Canadian Journal of Chemical Engineering 98, 1607–1621. doi:10.1002/cjce.23719.

Prasser, H.M., Böttger, A., Zschau, J., 1998. A new electrode-mesh tomograph for gas–liquid flows. Flow Measurement and Instrumentation 9, 111–119. doi:10.1016/S0955-5986(98)00015-6.

Schlegel, F., Bilde, K., Draw, M., Evdokimov, I., Hänsch, S., Kamble, V., Khan, H., Krull, B., Lehnigk, R., Li, J., Lyu, H., Meller, R., Petelin, G., Kota, S.P., Tekavčič, M., 2022. HZDR multiphase addon for OpenFOAM. Rodare. doi:10.14278/rodare.1877. Ver. 10-s.1-hzdr.2.

Vishwakarma, V., Schleicher, E., Bieberle, A., Schubert, M., Hampel, U., 2021. Advanced flow profiler for two-phase flow imaging on distillation trays. Chemical Engineering Science 231, 116280. doi:10.1016/j.ces.2020.116280.

Vishwakarma, V., Schubert, M., Hampel, U., 2018. Assessment of separation efficiency modeling and visualization approaches pertaining to flow and mixing patterns on distillation trays. Chemical Engineering Science 185, 182–208. doi:10.1016/j.ces.2018.03.052.

Waldrop, M.M., 2016. More than Moore. Nature 530, 145–147. doi:10.1038/530144a.

Wiedemann, P., Döß, A., Schleicher, E., Hampel, U., 2019. Fuzzy flow pattern identification in horizontal air-water two-phase flow based on wire-mesh sensor data. International Journal of Multiphase Flow 117, 153–162. doi:10.1016/j.ijmultiphaseflow.2019.05.004.

Wiedemann, P., Kota, S.P., Weckesser, S., Schleicher, E., Schubert, M., Hampel, U., 2022. Numerical simulation of the two-phase flow at a single trapezoid fixed valve using a hybrid CFD approach, in: The 12th international conference on Distillation & Absorption 2022, Toulouse. pp. 1–6.

Wörner, M., 2012. Numerical modeling of multiphase flows in microfluidics and micro process engineering: a review of methods and applications. Microfluid Nanofluid 12, 841–886. doi:10.1007/s10404-012-0940-8.

Zarei, T., Rahimi, R., Zivdar, M., 2009. Computational fluid dynamic simulation of mvg tray hydraulics. Korean Journal of Chemical Engineering 26, 1213–1219. doi:10.1007/s11814-009-0214-7.

Zhao, H., Li, L., Jin, J., Li, Q., 2018. Cfd simulation of sieve-fixed valve tray hydrodynamics. Chemical Engineering Research and Design 129, 55–63. doi:10.1016/j.cherd.2017.10.034.

Štrubelj, L., Tiselj, I., 2011. Two-fluid model with interface sharpening. International Journal for Numerical Methods in Engineering 85, 575–590. doi:10.1002/nme.2978.